Korean J. Chem. Eng., 38(10), 2134-2140 (2021)
DOI: 10.1007/s11814-021-0849-6

pISSN: 0256-1115
eISSN: 1975-7220

Oxygen-vacancy-rich spinel $CoFe_2O_4$ nanocrystals anchored on cage-like carbon for high-performance oxygen electrocatalysis

Yan-Chun Li*, Fan-Long Jin,†, and Soo-Jin Park***,†**

*Department of Chemistry and Pharmaceutical Engineering, Jilin Institute of Chemical Technology, Jilin City 132022, P. R. China
**Department of Polymer Materials, Jilin Institute of Chemical Technology, Jilin City 132022, P. R. China
***Department of Chemistry, Inha University, Nam-gu, Incheon 22212, Korea
(*Received 14 January 2021 • Revised 10 May 2021 • Accepted 18 May 2021*)

Abstract−We report spinel-type $CoFe_2O_4$ nanocrystals (NCs) synthesized through facile hydrothermal growth and their attachment on a cage-like carbon (CC) for efficient and durable oxygen evolution/reduction reaction (OER/ORR) performance. As a catalyst, the so-constructed $CoFe_2O_4$ NCs show significantly higher OER performance than bare $CoFe_2O_4$ and CC, leading to an overpotential of 1.59 V for the OER at a current density of 10 mA/cm. Furthermore, $CoFe_2O_4$ NCs on CC electrodes also exhibit good ORR performance, which is comparable to Pt/C, significantly higher than that of bare carbon fiber paper, and acts as a bifunctional electrocatalyst. The $CoFe_2O_4$ NCs anchored on the CC electrodes exhibit remarkably long-term stability, which is evaluated by continuous cycling (over 5,000 cycles), without any morphological change, but preserving all the materials within the electrode. The results indicate that the $CoFe_2O_4$ NCs have a promising potential for efficient, cost-effective, and durable oxygen electrocatalysis at large scales using earth-abundant materials and low-cost fabrication processes.

Keywords: $CoFe_2O_4$, Nanocrystals, Cage-like Carbon, Electrocatalysis

INTRODUCTION

To address the pressing concerns regarding increasing global energy demand, the development of energy storage systems with high power density from abundant materials has gained world-wide interest. Lithium-ion batteries (LIBs) are traditionally considered as one of the most promising candidates for use in electric vehicles owing to their high cycle capability and energy efficiency; however, their insufficient gravimetric storage capacity (100-200 W·h/kg) cannot meet the ever-growing demand for long-term application [1-4]. Much effort has been devoted to overcoming this limitation of the LIBs. For example, rechargeable metal-air batteries have attracted attention due to their extremely high gravimetric energy density, low cost, and environment-friendly operation [5-9]. Unfortunately, the rechargeable metal-air batteries are still at their early stages of development since there are some critical issues, such as limited life, high cost, and lack of bifunctional catalysts, that are yet to be addressed [10-12]. Thus, exploring metal-oxide-based bifunctional catalysts, which can satisfactorily catalyze both the oxygen reduction reaction (ORR) and oxygen evolution reaction (OER) upon discharging and charging, respectively, has become an urgent task.

Transition-metal oxides have drawn significant interest because of their sufficiently good stability and abundance (relative to the platinum group metals) [13-16]. As one of the representative binary metal oxides, $CoFe_2O_4$ has been widely studied in electrocatalysis owing to its high theoretical capacity of 916 mA·h/g [17-22]. Recently, various $CoFe_2O_4$ have been exploited using the soft template method [23], calcination method [24], and metal organic framework (MOF) conversion method [25]. In this regard, $CoFe_2O_4$ has been considered as a bifunctional oxygen electrocatalyst.

The electrochemical performance of electrocatalysts in metal-air batteries can be significantly enhanced not only by modifying their surface chemistry, but also by fabricating nanostructures. In recent years, coordination cages with controlled shape and high surface area have been actively pursued as a class of fundamental materials with a myriad of applications owing to their unique physicochemical properties. The applications include gas storage and separation [26], catalysis [27], sensing [28], biochemical applications [29], and many others [30,31].

In particular, the cages possess specific one-dimensional hollow nanostructures, which endow the cages with more open channels for electrons to migrate rapidly. More importantly, depositing abundant transition-metal oxides on the cages to obtain bifunctional oxygen electrocatalysts can prevent deactivation of metal oxides through irreversible oxidation during catalytic processes [32]. Moreover, the long-term stability of a catalyst electrode is also of significant importance in facilitating practical applications.

Herein, we report successful fabrication of high-performance bifunctional oxygen-involving electrocatalysts through a facile hydrothermal growth and their attachment on cage-like carbon (CC). The so-constructed catalysts significantly enhance the catalytic activity with good stability toward both the OER and ORR due to the enhanced interaction between $CoFe_2O_4$ nanocrystals (NCs) and

†To whom correspondence should be addressed.
E-mail: jinfanlong@163.com, sjpark@inha.ac.kr

CC support, which favors the modification of electronic states and high dispersion for active oxygen vacancies (i.e., Co/Fe-C species) during the ORR and OER processes.

EXPERIMENTAL

1. Materials

Iron (III) nitrate nonahydrate ($Fe(NO_3)_3{\cdot}9H_2O$) and cobalt nitrate hexahydrate ($Co(NO_3)_2{\cdot}6H_2O$) were purchased from Sigma-Aldrich Chemical Reagent Co. Magnesium carbonate hydroxide pentahydrate was obtained from Aladdin Reagent (Shanghai) Co., Ltd. Anhydrous ethanol was used as a solvent and supplied by Tianjin Dingshengxin Chemical Industry Co., Ltd. (China).

2. Preparation of Support and Electrocatalysts

The CC support was prepared by an MgO template method using benzene as a precursor, similar to a previous report [33].

$CoFe_2O_4$/CC electrocatalysts were prepared by a facile solvothermal approach. In a typical procedure, CC (55 mg) was dispersed ultrasonically in anhydrous ethanol (50 mL) for 1 h. Further, an ethanol solution (20 mL) containing $Fe(NO_3)_3{\cdot}9H_2O$ (0.0808 g, 0.2 mmol) and $Co(NO_3)_2{\cdot}6H_2O$ (0.0291 g, 0.1 mmol) was added to the CC suspension with vigorous stirring for 30 min. The mixture was transferred to a Teflon-lined autoclave and then reacted at 180 °C for 24 h. After cooling to the ambient temperature, the product was filtrated, repeatedly washed with anhydrous ethanol and de-ionized water, vacuum dried at 60 °C overnight, and finally annealed at 500 °C in Ar atmosphere for 2 h. Similarly, pristine $CoFe_2O_4$ as control was synthesized without any support.

3. Characterization

The structure and composition of the samples were characterized by X-ray diffraction (XRD, Bruker D8 Advance A25, Co $K_{\alpha 1}$ radiation of 1.78897 Å with an Fe filter of 0.02 mm thickness); transmission electron microscopy (TEM, JEM-2100F operating at 200 kV, equipped with scanning TEM (STEM) and energy dispersive X-ray (EDX) spectrometry); and X-ray photoelectron spectroscopy (XPS, ULVAC-PHI INC, PHI 5000 VersaProbe, Al K_α). The binding energy (E_b) of the XPS spectrum was in reference to C_{1s} at 284.6 eV. Thermogravimetric analysis (TGA, Netzsch STA449F3) was performed in 8 vol% O_2-containing Ar flow at 20 standard cubic centimeter per minute at a ramping rate of 10 °C/min. A Tristar II 3020 specific surface area analyzer was used to measure the BET surface areas of the $CoFe_2O_4$ NCs.

4. Electrochemical Measurement

Electrochemical experiments were conducted at 25 °C with a CHI 760E workstation (CH Instruments, USA) coupled with a modulated speed rotator electrode rotator (Pine Instrument Co., USA) in a three-electrode electrochemical cell using a sample-modified glassy carbon electrode as the working electrode, Ag/AgCl (3.0 mol/L KCl) as the reference electrode, and a platinum wire as the counter electrode. To prepare electrocatalyst inks, the catalyst (2.0 mg) and 5 wt% Nafion solution (50 μL) were ultrasonically dispersed in a water/ethanol (4 : 1, V/V, 1.0 mL) mixed solvent for 30 min. Consequently, a homogeneous ink was obtained. Further, the ink (15 μL) was loaded onto a glassy carbon electrode of diameter 4.0 mm. For comparison, a commercial Pt/C (20%, Johnson Matthey) electrode was prepared in the same manner. Linear sweep voltammogram (LSV) was performed in the potential range from 1.0 to 0 V (vs. Ag/AgCl, 3.0 mol/L KCl) at a scan rate of 10 mV/s in the N_2-saturated or O_2-saturated 0.1 mol/L KOH solution.

For the zinc-air battery test, the air electrode was prepared by uniformly coating the electrocatalyst ink on a carbon cloth (0.5 mg/cm^2) and then drying it at 80 °C for 2 h. Furthermore, a zinc foil was used as the anode. Both the electrodes were assembled into a home-made zinc-air battery, and a 6.0 mol/L KOH aqueous solution was used as the electrolyte. The battery tests were performed on an as-fabricated cell at room temperature with a multichannel potentiostat (LANHE CT2001A, Wuhan) and a constant discharge current mode (20 mA/cm^2). The tests were conducted until the voltages of the batteries dropped to 0 V.

The external biasing potentials used here are versus Hg/HgO RE or reversible hydrogen electrode (RHE). The biasing potentials versus Hg/HgO RE ($E^o_{Hg/Hg}$) were converted to potentials versus RHE (E_{RHE}) using the Nernst equation [34]:

$$E_{RHE} = E_{Hg/HgO} + 0.059 \times E^0_{Hg/HgO}\ (V) \quad (1)$$

where pH is the electrolyte pH and $E^0_{Hg/HgO}$=0.098 V versus normal hydrogen electrode (NHE) at 25 °C for the Hg/HgO/1.0 M NaOH (CH Instruments, Inc.). The OER overpotential (η) was calculated using the following equation:

$$\eta = E_{Hg/HgO} - E^0_{O_2/H_2O}\ (V) \quad (2)$$

where $E^0_{O_2/H_2O}$ is the thermodynamic potential for water oxidation relative to Hg/HgO at pH=13.97, which was calculated as follows:

$$E^0_{O_2/H_2O} = 1.23 - 0.059 \times pH - E^0_{Hg/HgO} = 1.23 - 0.059 \times 13.97 - 0.098 = 0.308\ (V)$$

The NHE overpotential was also calculated using Eq. (2) considering $E^0_{H^+/H_2}$ instead of $E^0_{O_2/H_2O}$, as shown in Eq. (3):

$$\eta = E_{Hg/HgO} - E^0_{H^+/H_2}\ (V) \quad (3)$$

where $E^0_{H^+/H_2}$ is the thermodynamic potential for water reduction relative to Hg/HgO at pH=13.97, which was calculated as follows:

$$E^0_{H^+/H_2} = -0.059 \times pH - E^0_{Hg/HgO} = -0.059 \times 13.97 - 0.098 = -0.922\ (V)$$

In this study, all the reported potentials and plots were considered without any IR correction, and the current densities were calculated using geometric surface areas.

RESULTS AND DISCUSSION

1. Structural Characterization of the $CoFe_2O_4$ NCs

The morphology of the $CoFe_2O_4$ NCs was investigated by TEM. Figs. 1(a) and (b) show the TEM image and particle size of statistics of the $CoFe_2O_4$ NCs. As shown in Figs. 1(a) and (b), carbon shows a large quantity of cage-like structures, and the $CoFe_2O_4$ NCs embedded in these structures have diameters of approximately 20 nm. As shown in Fig. 1(b), the magnified TEM image of a single $CoFe_2O_4$ nanoparticle clearly displays typical lattice-fringe spacing of 0.255 nm, corresponding to the plane of the $CoFe_2O_4$ crystal (311 nm), which reveals the presence of crystalline $CoFe_2O_4$ crystal lattices [35,36].

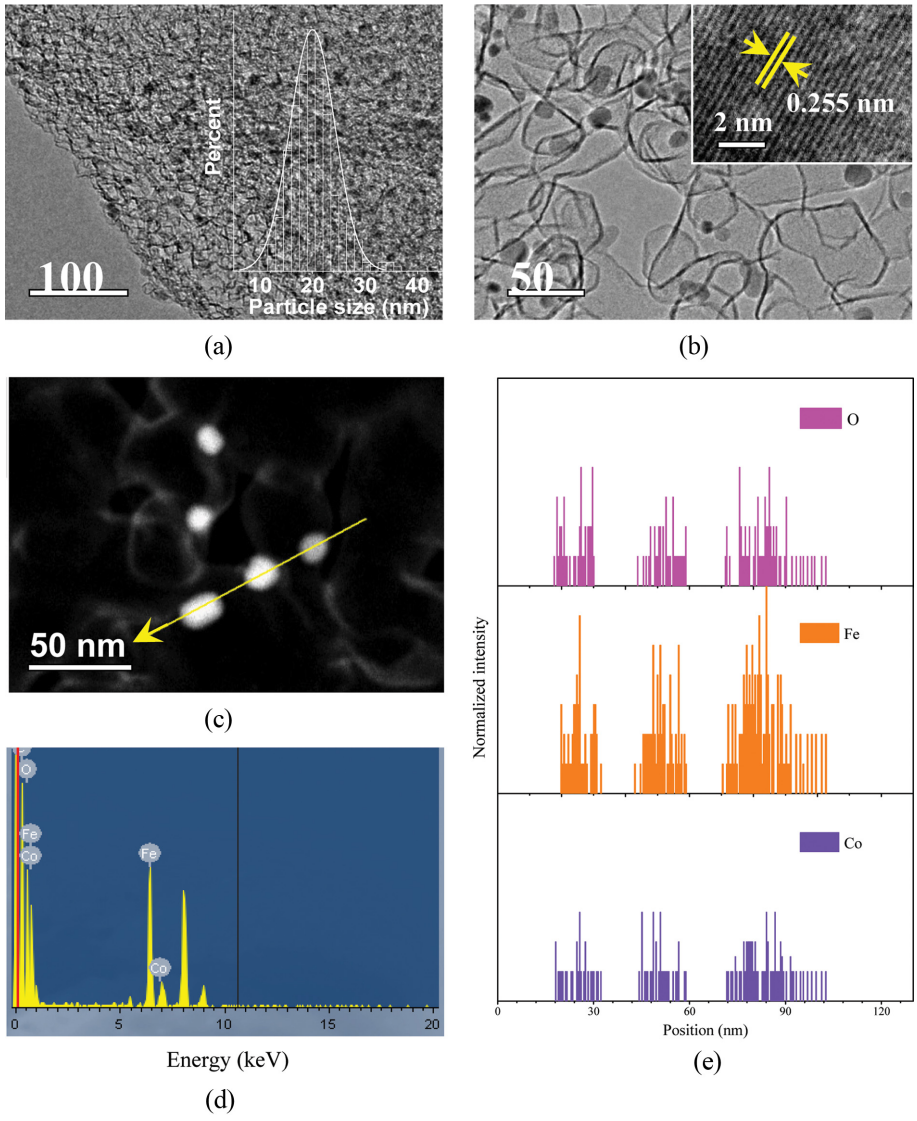

Fig. 1. (a) TEM image and particle size of statistics, (b) Magnified TEM image, (c) STEM image of $CoFe_2O_4$ NCs, (d) EDX mapping of $CoFe_2O_4$ NCs, (e) Elemental analysis of $CoFe_2O_4$ NCs.

The STEM image of $CoFe_2O_4$ NCs is indicated in Fig. 1(c), which further verifies the uniform distribution of the $CoFe_2O_4$ NCs on the surface of CC, and the $CoFe_2O_4$ NCs are composed of sub-clusters of size 20 nm.

The EDX mapping of $CoFe_2O_4$ NCs is presented in Fig. 1(d). The peaks at approximately 0.7 and 6.4 keV are attributed to Fe and the peaks at around 0.6 and 7 keV are attributed to Co. The results demonstrate the formation of the $CoFe_2O_4$ NCs. The existence of the Co and Fe elements in the $CoFe_2O_4$ NCs is further evident from the elemental analysis, as shown in Fig. 1(e).

Fig. 2(a) shows the nitrogen absorption/desorption isotherm of $CoFe_2O_4$ NCs. The nitrogen isotherm exhibits a type IV nitrogen sorption isotherm with a large surface area (ca. 900 m^2/g) and hierarchical pore features [37].

The pore size distribution of $CoFe_2O_4$ NCs is indicated in Fig. 2(b). The corresponding pore size distribution plot confirms the coexistence of micro-meso-macro-porous structure.

The XRD patterns of CC, $CoFe_2O_4$, and $CoFe_2O_4$ NCs are presented in Fig. 3. The observed characteristic peaks of $CoFe_2O_4$ and $CoFe_2O_4$ NCs are in clear correspondence with the cubic spinel phase of $CoFe_2O_4$ (PDF-#22-1086). Moreover, the labeled peaks at 30.1°, 35.44°, 56.97°, and 62.59° are in good agreement with the (220), (311), (511), and (440) facets, respectively, thereby indicating the formation of single-phase $CoFe_2O_4$ [38,39]. There are no noticeable peaks in the XRD profile of unannealed $CoFe_2O_4$ NCs, thus suggesting that the structures of the $CoFe_2O_4$ NCs are almost amorphous or have low crystallinity [40].

Furthermore, TGA was performed to display the decomposition behavior of the $CoFe_2O_4$ NCs. As shown in Fig. 4, obvious weight loss between 400-500 °C occurred due to the decomposition of $Fe(NO_3)_3{\cdot}9H_2O$ and $Co(NO_3)_2{\cdot}6H_2O$. Therefore, an annealing temperature of 400 °C was considered.

Further, XPS characterization was performed to analyze the elemental composition and surface valence states of the $CoFe_2O_4$ NCs.

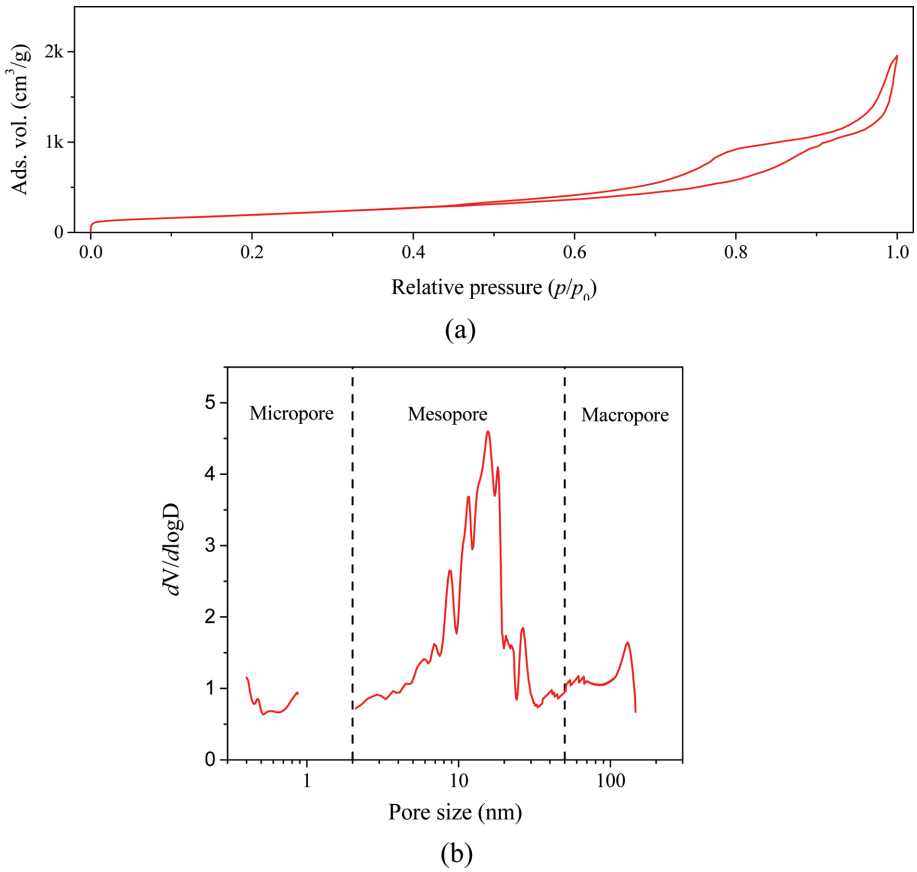

Fig. 2. (a) Nitrogen adsorption/desorption isotherms of $CoFe_2O_4$ NCs; (b) Pore size distribution of $CoFe_2O_4$ NCs.

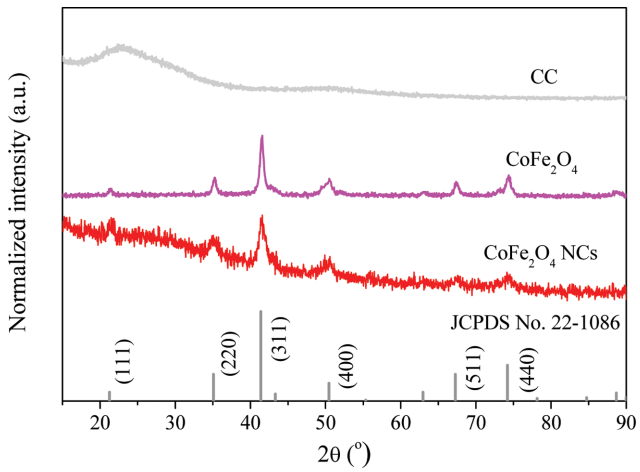

Fig. 3. XRD patterns of $CoFe_2O_4$ NCs.

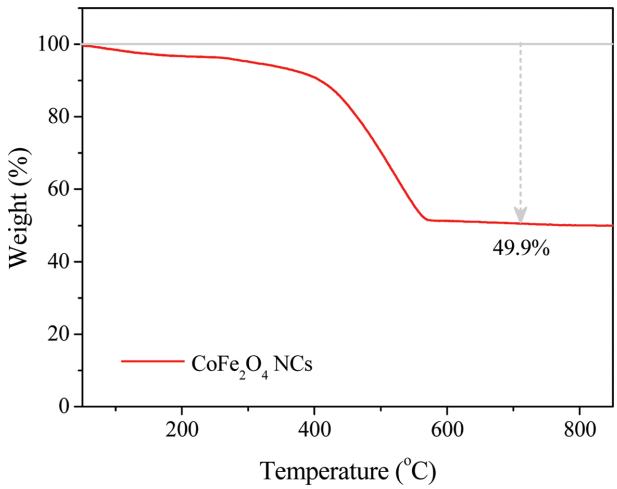

Fig. 4. TGA thermogram of $CoFe_2O_4$ NCs.

As shown in Fig. 5(a), besides the C_{1s} signal originating from the adventitious carbon, the survey XPS spectrum indicates the presence of the Co, Fe, and O elements. There are four peaks in the XPS spectrum of Co_{2p}, as shown in Fig. 5(b). The first two peaks located at 780.7 eV and 786.1 eV correspond to $Co_{2p3/2}$ and its shake-up satellite, respectively, while the other two peaks at 796.1 eV and 803.3 eV can be assigned to $Co_{2p1/2}$ and its shake-up satellite, respectively [41]. The results reveal that cobalt exists in the +2 oxidation state in the sample. The Fe_{2p} XPS spectrum (Fig. 5(c)) shows double peaks located at 711.3 eV and 724.9 eV that correspond to the peaks of $Fe_{2p3/2}$ and $Fe_{2p1/2}$ from the Fe_{2p} energy level, thereby indicating the presence of Fe^{3+} cations. The O_{1s} spectrum is divided into two peaks (Fig. 5(d)) located at approximately 529.1 eV and 531.2 eV, and these peaks can be attributed to crystal lattice oxygen (O-Fe-O) and surface hydroxyl groups (OH-O), respectively [42]. This result further proves the formation of $CoFe_2O_4$ through

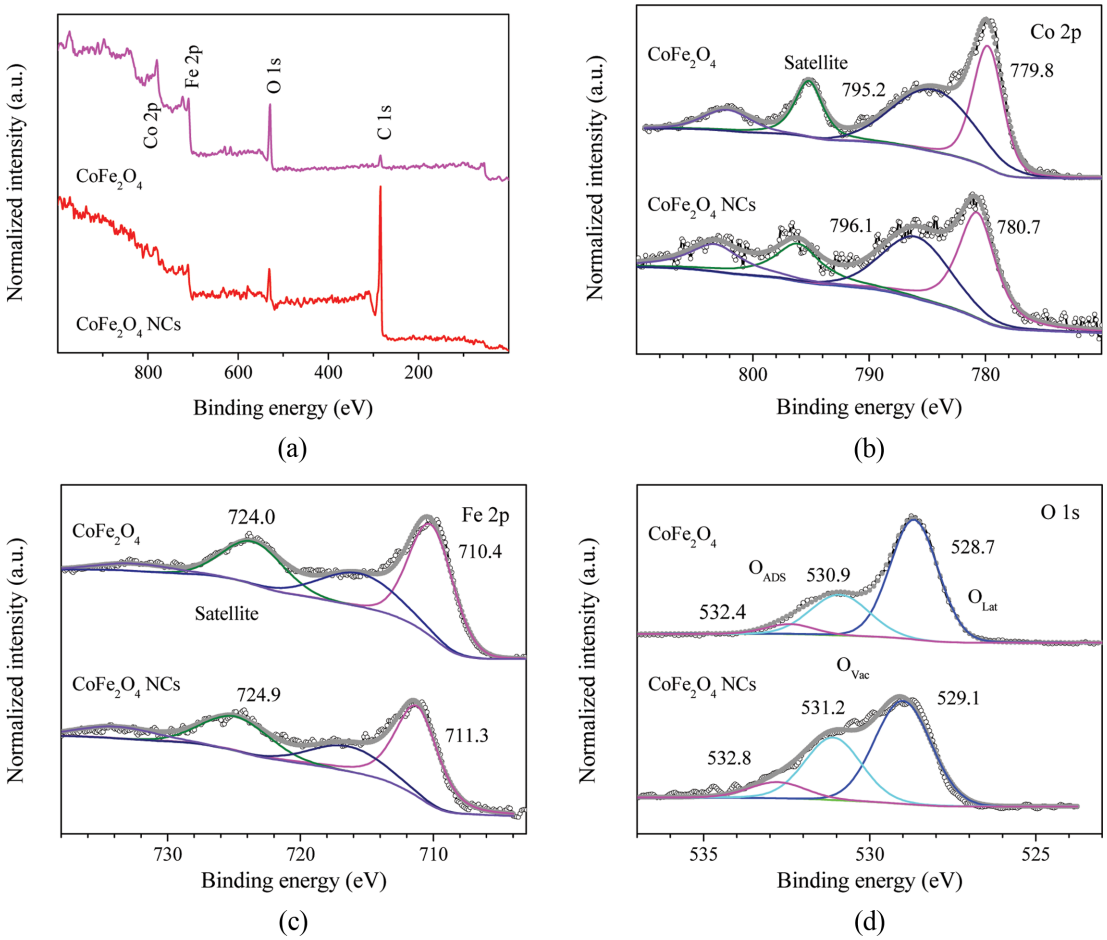

Fig. 5. XPS spectra of $CoFe_2O_4$ NCs: (a) survey spectrum, (b) high-resolution Co_{2p}, (c) high-resolution Fe_{2p}, (d) high-resolution O1s.

this strategy.

As shown in Fig. 5(d), the O_{1s} peak at 529.1 eV is associated with the crystal lattice oxygen (O_{Lat}), the O_{1s} peak at 532.8 eV is ascribed to the adsorbed oxygen (O_{Ads}) on the surface of the samples, and the O_{1s} peak at 531.2 eV is attributed to the oxygen vacancy (O_{Vac}) regions of the samples [43-45]. The O_{Vac} values of $CoFe_2O_4$ and the $CoFe_2O_4$ NCs calculated from Fig. 5(d) were 21.9% and 37.8%, respectively. The O_{Vac} value of the $CoFe_2O_4$ NCs is great higher than that of $CoFe_2O_4$. This indicates the existence of a large amount of oxygen vacancies in the $CoFe_2O_4$ NCs.

2. Electrocatalytic Performance of the $CoFe_2O_4$ NCs

Fig. 6(a) shows the capacitance-corrected ORR activity of the $CoFe_2O_4$ NCs compared to CC, $CoFe_2O_4$, and the reference Pt/C 20%, which consists of 20 wt% Pt and 80 wt% Vulcan XC-72 (E-tek). As shown in Fig. 6(a), the onset potentials for the ORR of the $CoFe_2O_4$ NCs are 0.86 V vs RHE, while CC, $CoFe_2O_4$, and Pt/C are at 0.76 V, 0.76 V, and 1.01 V vs RHE, respectively. Compared to the limiting currents of CC and $CoFe_2O_4$ of −2.9 and −3.6 A/cm, respectively, the value of the limiting current of the $CoFe_2O_4$ NCs is found to be −0.51 A/cm as the particle size approaches the nano scale, thereby indicating optimal coverage and mass transport of the $CoFe_2O_4$ NCs [46].

Fig. 6(b) shows the capacitance-corrected OER activity of the $CoFe_2O_4$ NCs compared to CC, $CoFe_2O_4$, Pt/C, and RuO. The polarization curves shown in Fig. 6(b) indicate that to reach a current density of 10 mA/cm, the $CoFe_2O_4$ NCs should have an overpotential of 1.59 V, which is smaller than that of RuO_2 (1.58 V).

This high OER performance of the $CoFe_2O_4$ NCs is further evident from the Tafel plots. The Tafel slope can be used to estimate the kinetics and mechanism of the OER. The smaller the Tafel slope, the better the OER kinetics [47,48]. Fig. 6(c) shows the Tafel slope of the $CoFe_2O_4$ NCs derived from the polarization curve compared to that of $CoFe_2O_4$, Pt/C, and RuO. The Tafel slope of the $CoFe_2O_4$ NCs is 68 mV/dec, which is much lower than that of $CoFe_2O_4$ or Pt/C and is slightly higher than that of RuO. These results indicate that the $CoFe_2O_4$ NCs have high OER performance.

Fig. 6(d) shows the stability test of the $CoFe_2O_4$ NCs for 5000 continuous potential cycles. The $CoFe_2O_4$ NCs are anchored on the CC electrodes exhibiting excellent long-term stability, which was evaluated by continuous cycling (over 5000 cycles), without any morphological change, as shown in Fig. 6(d).

The remarkable ORR and OER performance of the $CoFe_2O_4$ NCs can be well understood based on our experimental characterization. As is known, $CoFe_2O_4$ itself exhibits low activity due to its very poor conductivity, while CC is a good metal-free catalyst with a large specific surface area and abundant defects. The strong

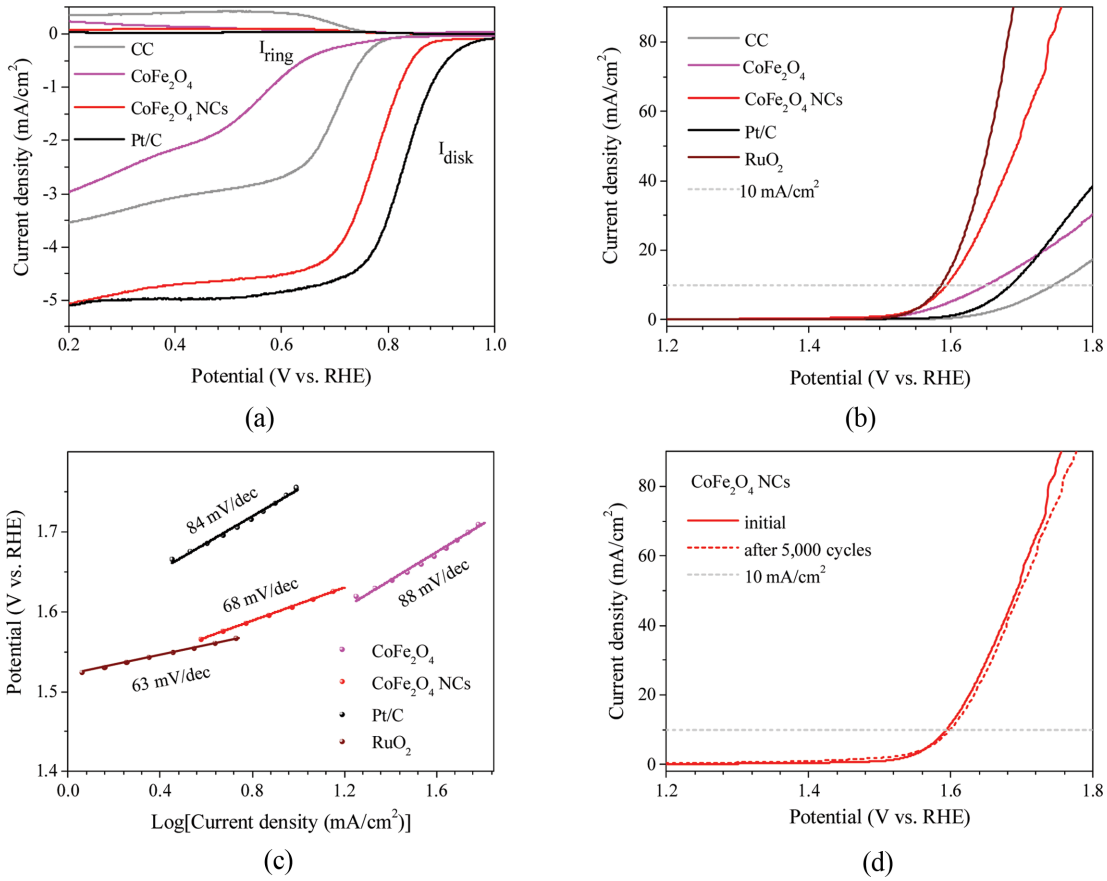

Fig. 6. (a) LSV curves of CC, $CoFe_2O_4$, Ne_2O_4 NCs, and Pt/C for ORR, (b) LSV curves of CC, $CoFe_2O_4$, Ne_2O_4 NCs, Pt/C, and RuO for OER, (c) Lowest Tafel slopes of $CoFe_2O_4$, Ne_2O_4 NCs, Pt/C, and RuO, (d) Stability test of $CoFe_2O_4$ NCs for 5,000 continuous potential cycling.

interaction between the $CoFe_2O_4$ NCs and CC support makes the interfacial oxygen vacancies (i.e., Co/Fe-C species) ORR- and OER-active, leading to the higher ORR and OER activity of the $CoFe_2O_4$ NCs than that of bare $CoFe_2O_4$ and CC.

CONCLUSIONS

We successfully prepared $CoFe_2O_4$ NCs via a facile hydrothermal growth and attached NCs on CC. The cage-like nanostructure was found to be favorable for enhancing the intrinsic catalytic activity of the bifunctional $CoFe_2O_4$/CC electrocatalyst, thus offering higher OER activity than that of bare $CoFe_2O_4$ and CC, and also better ORR performance than that of Pt/C and bare carbon fiber paper. The enhanced interaction favors the modification of electronic states and high dispersion for active oxygen vacancies (i.e., Co/Fe-C species) during the oxygen reduction and evolution processes, which plays a key role in boosting the electrocatalytic performance.

ACKNOWLEDGEMENTS

This work was supported by the Technology Innovation Program (or Industrial Strategic Technology Development Program-Development of technology on materials and components) (20010106, Adhesives with low water permeability and low outgassing) funded by the Ministry of Trade, Industry & Energy (MOTIE, Korea).

REFERENCES

1. T. Y. Ma, S. Y. Wu and F. Wang, *ACS Appl. Mater. Interfaces*, **50**, 56086 (2020).
2. K. Y. Zou, N. Li, Y. Z. Chen and J. J. Sun, *ACS Appl. Nano Mater.*, **6**, 5732 (2020).
3. Q. Y. Liu, X. Y. Yi and X. Han, *Fire Technol.*, **56**, 2509 (2020).
4. R. H. Tammam, A. M. Fekry and M. M. Saleh., *Korean J. Chem. Eng.*, **11**, 1932 (2019).
5. Y. Zhan, C. H. Xu and J. Y. Lee, *J. Mater. Chem. A*, **2**, 16217 (2014).
6. A. Muthurasu, B. Dahal and H. Y. Kim, *ACS Appl. Mater. Interfaces*, **37**, 41704 (2020).
7. E. Davari and D. G. Ivey, *Sustain. Energy Fuels*, **2**, 39 (2018).
8. S. S. Shinde, C. H. Lee and J. H. Lee, *ACS Nano*, **1**, 347 (2017).
9. S. X. Yang, Y. H. Yu and M. L. Dou, *Angew. Chem.*, **41**, 14866 (2019).
10. L. Sharma, R. Gond and P. Barpanda, *ACS Catal.*, **1**, 43 (2020).
11. J. T. Ren and Z. Y. Yuan, *ACS Sustain. Chem. Eng.*, **11**, 11121 (2019).
12. D. U. Lee, P. Xu and Z. W. Chen, *J. Mater. Chem. A*, **4**, 7107 (2016).
13. K. E. Fritz, Y. C. Yan and J. Suntivich, *Nano Res.*, **12**, 2307 (2019).
14. D. D. Wang, X. Chen and W. S. Yang, *Nanoscale*, **5**, 5312 (2013).
15. R. H. Tammam, A. M. Fekry and M. M. Saleh, *Korean J. Chem.*

Eng., **36**, 1932 (2019).
16. D. Takimoto, K. Fukuda and W. Sugimoto, *Electrocatalysis*, **8**, 144 (2017).
17. Q. M. He, R. Kun and Z. Y. Wen, *ACS Appl. Mater. Interfaces*, **9**, 36927 (2017).
18. W. Bian, Z. Yang and R. Yang, *J. Power Sources*, **250**, 196 (2014).
19. J. Yin, L. Shen and P. X. Xi, *J. Mater. Res.*, **33**, 590 (2018).
20. C. P. Wang, H. Su and J. M. Zhang, *ACS Appl. Mater. Interfaces*, **10**, 28679 (2018).
21. H. B. Wu and X. W. Lou, *Sci. Adv.*, **3**, 9252 (2017).
22. H. S. Fan, Y. F. Zhang and J. Xu, *Nano Energy*, **33**, 168 (2017).
23. J. G. Kim, Y. Noh and S. Lee, *Nanoscale*, **9**, 5119 (2017).
24. K. Alireza, Y. Serdar and R. B. Prabhakar, *ACS Appl. Mater. Interfaces*, **7**, 17851 (2015).
25. Z. X. Wu, H. B. Wu and W. Jin, *ACS Sustain. Chem. Eng*., **24**, 9226 (2020).
26. C. J. Liu, Z. C. Zhang and G. J. Guo, *RSC Adv.*, **6**, 106443 (2016).
27. K. N. Chee, W. T. Ren and J. Wu, *Chem. Sci*., **10**, 1549 (2019).
28. Y. F. Bing, Y. Zeng and W. T. Zheng, *Nanoscale*, **7**, 3276 (2015).
29. A. Nazir, A. Y. Hussein and V. Francis, *Chem. Soc. Rev*., **44**, 9 (2015).
30. R. Martin, G. N. Martin and B. Nico, *Chem. Soc. Rev*., **45**, 6213 (2016).
31. B. Marco, P. S. Raul and H. Maciej, *Mol. Syst. Des. Eng*., **4**, 912 (2019).
32. H. G. Wang, D P. Liu and Q. Duan, *Mater. Lett*., **172**, 64 (2016).
33. K. Xie, X. T. Qin and Y. N. Wang, *Adv. Mater*., **24**, 347 (2012).
34. A. Kargar, S. Yavuz and T. K. Kim, *ACS Appl. Mater. Interfaces*, **3**2, 17851 (2015).
35. Q. M. He, K. Rui and C. H. Chen, *ACS Appl. Mater. Interfaces*, **42**, 36927 (2017).
36. K. Praveena and M. Bououdina, *J. Electron. Mater*., **49**, 6187 (2020).
37. L. J. Abbott and C. M. Colina, *J. Chem. Eng. Data*, **10**, 3177 (2014).
38. S. Safran, F. Bulut and A. R. A. Nefrow, *J. Mater. Sci: Mater. El*., **31**, 20578 (2020).
39. B. Verma and C. Balomajumder, *Korean J. Chem. Eng*., **37**, 1157 (2020).
40. Y. Georgioua, I. T. Papadas and G. S. Armatas, *Environ. Sci.: Nano*, **6**, 1156 (2019).
41. Y. Ding, J. Zhao and F. C. Yang, *ACS Appl. Energy Mater*., **2**, 1026 (2019).
42. X. Wang, L. Z. Zhuang and P. Yuan, *Chem. Res. Chinese U*., **36**, 479 (2020).
43. M. Saha, S. Ghosh, S. Paul, B. Dalal and S. K. De, *ChemistrySelect*, **3**, 6654 (2018).
44. T. Chen, J. Meng, Q. Lin, X. Wei, J. Li and Z. Zhang, *J. Alloys Compd*., **780**, 498 (2019).
45. S. Li, M. Wang, C. Li, J. Liu, M. Xu, J. Liu and J. Zhang, *Sci. China Mater*., **61**, 1085 (2018).
46. G. Lavorato, E. Lima and E. Winkler, *J. Phys. Chem. C*, **5**, 3047 (2018).
47. D. Guo, J. Wang, L. Zhang, X. Chen, Z. Wan and B. Xi, *Small*, 2002432 (2020).
48. S. L. Zhang, B. Y. Guan, X. F. Lu, S. Xi, Y. Du and X. W. Lou, *Adv. Mater*., **32**, 2002235 (2020).